The Astrophysical Journal, 952:54 (10pp), 2023 July 20 https://doi.org/10.3847/1538-4357/acdb4f

Optical and Near-infrared Continuum Emission Region Size Measurements in the Lensed Quasar FBQ J0951+2635

Angelica B. Rivera[1], Christopher W. Morgan[1], Steven M. Florence[1], Scott E. Dahm[2], Frederick J. Vrba[2], Trudy M. Tilleman[2], Matthew A. Cornachione[3], and Emilio E. Falco[4]
[1] Department of Physics, United States Naval Academy, 572C Holloway Rd., Annapolis, MD 21402, USA; abrivera@upenn.edu
[2] United States Naval Observatory, Flagstaff Station, 10391 West Naval Observatory Rd., Flagstaff, AZ 86005, USA
[3] Oregon Institute of Technology, 3201 Campus Dr., Klamath Falls, OR 97601, USA
[4] Harvard-Smithsonian Center for Astrophysics, 60 Garden St., Cambridge, MA 02138, USA

Received 2022 July 7; revised 2023 May 12; accepted 2023 May 25; published 2023 July 18

Abstract

We present 10 seasons of Sloan Digital Sky Survey *r*-band monitoring observations and five seasons of *H*-band observations of the two-image system FBQ J0951+2635 from the Kaj Strand Astrometric Reflector at the United States Naval Observatory, Flagstaff Station. We supplement our light curves with six seasons of monitoring data from the literature to yield a $10 + 6$ season combined data set, which we analyzed with our Monte Carlo microlensing analysis routine to generate constraints on the structure of this system's continuum emission source and the properties of the lens galaxy. Complementing our optical light curves with the five-season near-infrared light curves, we ran a joint Monte Carlo analysis to measure the size of the continuum emission region at both wavelengths, yielding $\log(r_{1/2}\,\mathrm{cm}^{-1}) = 16.24^{+0.33}_{-0.36}$ in the r band and $17.04^{+0.26}_{-0.30}$ in the H band at rest wavelengths of 2744 and 7254 Å, respectively, correcting for an assumed inclination angle of 60°. Modeling the accretion disk temperature profile as a power law $T(r) \propto r^{-\beta}$, we successfully constrain the slope for FBQ J0951+2635 to $\beta = 0.50^{+0.50}_{-0.18}$, shallower than, but nominally consistent with, the predictions of standard thin-disk theory, $\beta = 0.75$.

Unified Astronomy Thesaurus concepts: Quasars (1319); Gravitational lensing (670); Gravitational microlensing (672); Quasar microlensing (1318)

Supporting material: machine-readable tables

1. Introduction

Since the optical and UV continuum emission source in quasars is not resolvable by conventional telescopes, several of the most basic properties of quasar accretion disks (e.g., physical size and temperature profile) remain weakly constrained. To date, only two observational techniques have been successfully employed to make quantitative measurements of the structure of the optical/UV continuum source: reverberation mapping (e.g., Edelson et al. 2015; Cackett et al. 2018) and the analysis of the signal from microlensing in gravitationally lensed quasars. There are two methods for performing the latter type of analysis. One method is to image a quasar in multiple bands at a single observing epoch, examining whether there is a significant wavelength dependence to the flux ratios or if there are deviations between the observed flux ratios and the predictions produced from macroscopic lens models (e.g., Pooley et al. 2007; Blackburne et al. 2011; Mosquera & Kochanek 2011). This "chromatic microlensing" technique has some weaknesses, however. The single-epoch technique requires an assumption of a prior for the mean mass for the lens galaxy stars, and it can only be used in systems with short time delays, since it is not possible to differentiate between intrinsic and extrinsic flux ratio anomalies in systems with longer delays. In the second method, multi-epoch light curves are collected to analyze changes in the magnification of the quasar images as they move across the complex network of magnification from the aggregated gravitational potential of the lens galaxy stars (see e.g., Kochanek et al. 2006; Dai et al. 2010; Hainline et al. 2012, 2013; Cornachione et al. 2020b, who employ the technique of Kochanek 2004). This method requires more observing time and cosmological modeling of the effective transverse velocity, but it does not require an assumption of the median mass of the stars in the lens galaxy.

Multi-epoch measurements of the continuum emission region from microlensing are reasonably consistent with those generated from reverberation mapping (Peterson et al. 2004, although see Paic et al. 2022 and Section 6 of this paper for a discussion of the potential biases in these techniques arising from reverberation of high-frequency intrinsic variability), but they can be two to four times as large as the radii calculated from magnification-corrected flux measurements when assuming a Shakura & Sunyaev (1973) thin disk (Morgan et al. 2010; Cornachione & Morgan 2020). Another discrepancy is that chromatic microlensing studies have not reached a consensus on the slope of the accretion disk temperature profile, β, where $T(r) = r^{-\beta}$. Although the Shakura & Sunyaev (1973) thin-disk model has been shown to be inconsistent with accretion disk observations, its analytic nature and its relative closeness to observations serve as helpful reference points. The temperature slope of a Shakura & Sunyaev (1973) thin disk is $\beta = 3/4$, but several single-epoch investigations have yielded a shallower slope $\beta \approx 0.5$ (Bate et al. 2018), while others find β to be much steeper ($\beta \approx 1.25$; Jiménez-Vicente et al. 2014). It has been shown, however, that the single-epoch method can produce an overly steep estimate of the temperature slope when the

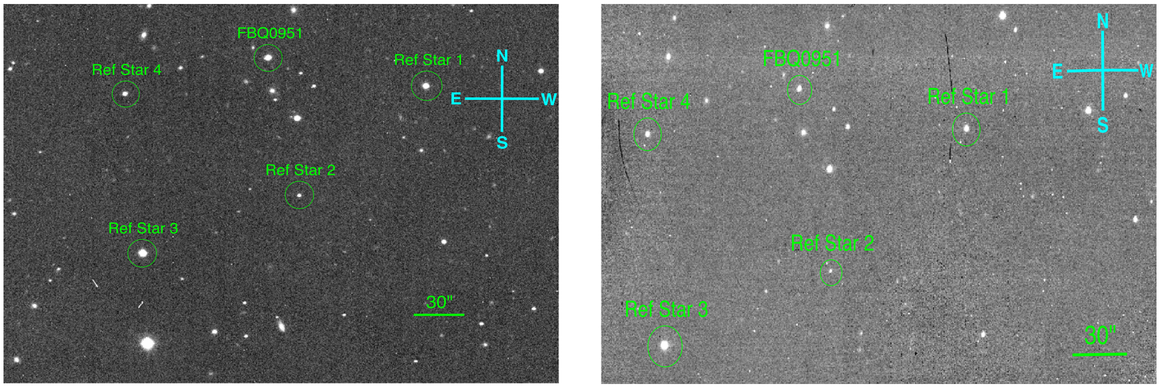

Figure 1. Left: NOFS r-band image of FBQ0951 taken with Tek2k using the 1.55 m Kaj Strand Astrometric Reflector. The four reference stars used in the data reduction are labeled. Right: NOFS H-band image of FBQ0951; the same reference stars chosen for the r-band data reduction are used and highlighted.

chromatic variation is weak (Bate et al. 2018). Measurements of β from reverberation mapping (Cackett et al. 2018; Edelson et al. 2019) are less tightly constrained, but they are on average consistent with simple thin-disk theory. Multi-epoch microlensing studies have consistently found β to be shallower than that of the Shakura & Sunyaev (1973) thin-disk model (Cornachione & Morgan 2020). This is consistent with the findings of Morgan et al. (2010), who found that β would need to be $\sim$0.5 to bring multi-epoch microlensing size measurements and flux-based size measurements into agreement.

The first empirical estimate of a lensed quasar's temperature profile using the multi-epoch approach was performed by Poindexter et al. (2008), who found $\beta = 0.61^{+0.21}_{-0.17}$ for the system HE 1104-1805 when analyzing optical and near-infrared (NIR) monitoring data. Cornachione et al. (2020a) used a similar technique to find somewhat shallower slopes when analyzing r- and H-band light curves for QJ0957+561 and SBSJ0909+532 ($\beta = 0.54^{+0.58}_{-0.22}$ and $\beta = 0.25^{+0.13}_{-0.06}$, respectively). A joint fit of the two systems yielded $\beta = 0.35^{+0.16}_{-0.08}$. For FBQ J0951+2635, we follow the methods of Cornachione et al. (2020a) to measure the size of the accretion disk in both of these bands by analysis of multi-epoch microlensing variability, and we calculate the corresponding temperature profile slope β.

In this paper, we present new optical r-band and NIR H-band light curves for FBQ J0951+2635 (Schechter et al. 1998; hereafter, FBQ0951), a two-image quasar system gravitationally lensed by an edge-on Sa- or Sb-type spiral galaxy. The observed properties of the quasars are as follows: the separation between the two quasar images is 1$''$1 with lens redshift $z_l = 0.26$ (Eigenbrod et al. 2007) and source redshift $z_s = 1.247$ (Sluse et al. 2012). The supermassive black hole powering FBQ0951 has a mass $M_{\rm BH} = 8.9 \times 10^8\,M_\odot$, as derived from the width of the Mg II line and the system's luminosity (Peng et al. 2006).

We use the Hubble Space Telescope (HST) H-band (F160W) photometry from the CASTLES survey (Lehár et al. 2000) to identify the quasar image and lens galaxy astrometry, since the separation between components is too small to permit resolution with our ground-based photometry. Example r- and H-band images from the US Naval Observatory, Flagstaff Station (NOFS), are shown in Figure 1, and in Figure 2 we display H-band images from HST that highlight both the system's astrometry and lens galaxy morphology. FBQ0951 is relatively unusual, in that it is lensed by an edge-on spiral galaxy, producing image A in the galactic halo and image B several scale heights above the galactic disk.

In Section 2, we detail our new optical and NIR observations of FBQ0951 from NOFS. In Section 3, we describe our model for strong lensing, and in Section 4 we describe our microlensing simulations. In Section 5, we describe the results of the microlensing simulations, and in Section 6 we discuss general conclusions and comparisons with the literature. The cosmological parameters we choose to use throughout this paper are $\Omega_M = 0.3$, $\Omega_\lambda = 0.7$, and $H_0 = 70$ km s^{-1} Mpc^{-1} (e.g., Planck Collaboration et al. 2020).

2. Data

2.1. Optical

2.1.1. New Optical Observations and Data Reduction

NOFS observations were performed with the 1.55 m Kaj Strand Astrometric Reflector at NOFS with either the 2048 × 2048 Tek2k or 2048 × 4096 EEV (*OneChip*) CCDs. The Tek2k observations were taken between 2008 March and 2017 April, and the *OneChip* observations from 2009 May through 2017 April. 300 s exposures were taken using both detectors. The pixel scale for Tek2k is 0$''$33 and for *OneChip* it is 0$''$18.

We first combine the subexposures from each night to make a single image. We use four reference stars for the analysis to identify the flux normalization and point-spread function (PSF) for each combined image. We held both the astrometry (determined by H-band HST imaging) and the galaxy flux constant over all epochs. We tested a range of galaxy fluxes and settled on the value that minimized the summed χ^2 in the residuals from the entire data set, following subtraction of the galaxy and quasar image PSF models. In total, there were 30 nights of data included with Tek2k and 34 nights included with *OneChip*. The reduced r-band NOFS light curves are provided in Table 1.

2.1.2. Optical Data from the Literature

In addition to the data we acquired from NOFS, we incorporated light curves published previously by Paraficz et al. (2006) and in the GLENDAMA database (Goicoechea et al. 2006). The Paraficz et al. (2006) data were taken with the Nordic Optical Telescope between 1998 and 2002, totaling 58 nights of data. The GLENDAMA light curves originate from two data sets. These included data from the Maidanak 1.5 m

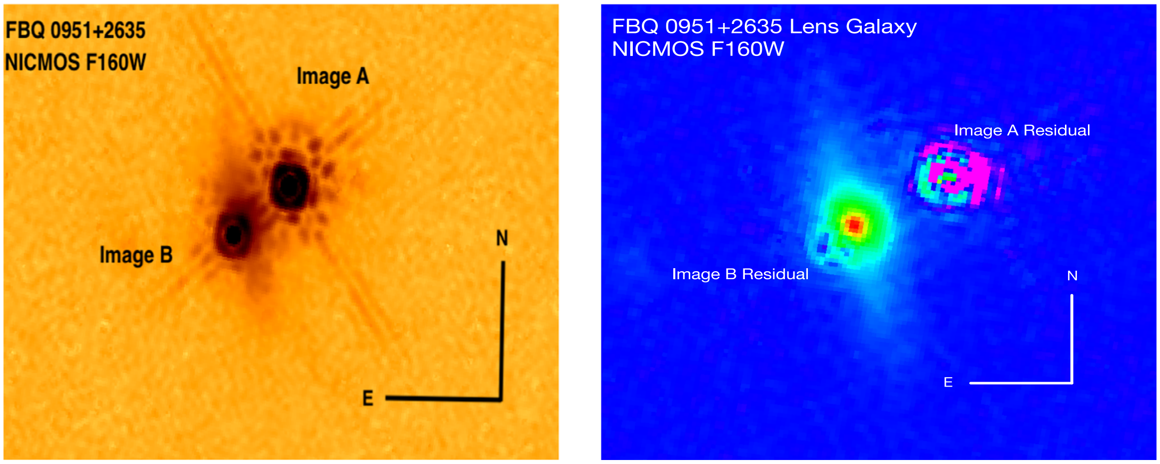

Figure 2. Left: HST *H*-band (F160W) image from CASTLES (Lehár et al. 2000). Right: the same HST image following subtraction of the flux from quasar images A and B. Some residuals from this subtraction are visible. Here, the edge-on spiral lens galaxy is clearly visible.

Table 1
r-band NOFS Light Curves for FBQ J0951+2635

HJD-2450000 (days)	Image A (mag)	Error A (mag)	Image B (mag)	Error B (mag)	Detector
4544.660	0.675	0.006	2.020	0.010	Tek2k
4561.707	0.676	0.006	1.988	0.010	Tek2k
4584.657	0.677	0.006	2.015	0.012	Tek2k
4613.676	0.669	0.002	2.047	0.006	Tek2k
4617.688	0.689	0.005	2.043	0.009	Tek2k
4792.984	0.640	0.006	2.031	0.012	Tek2k
4829.842	0.625	0.006	2.031	0.014	Tek2k
4833.874	0.614	0.007	2.032	0.015	Tek2k
4862.863	0.634	0.006	1.973	0.010	Tek2k
4883.914	0.612	0.007	2.094	0.017	Tek2k
4911.779	0.644	0.006	1.951	0.009	Tek2k
4964.699	0.651	0.001	1.954	0.002	OneChip
4997.657	0.629	0.007	1.985	0.018	OneChip
5201.930	0.621	0.007	2.055	0.017	Tek2k
5208.978	0.629	0.006	1.995	0.011	Tek2k

Note. A portion of this table is shown to demonstrate its form and content. The table in its entirety is available in machine-readable form in the online journal article.

(This table is available in its entirety in machine-readable form.)

AZT-22 Telescope collected from 2001 April to 2006 April for a total of 37 nights (Shalyapin et al. 2009), as well as 2 m Liverpool Robotic Telescope (LRT) observations from 2009 April through 2016 March, totaling 29 nights (Gil-Merino et al. 2018). From 2009 to 2012, the LRT observations were made using RATCam, with three consecutive exposures of 300 s per night, and from 2013 to 2016 the data were taken with the IO:O camera, with two 250 s exposures per night. The pixel scale for both modes of observation was $0\farcs3$.

In constructing the final combined light curves, our Tek2k light curve was the base to which the other sources of data were calibrated. The offset in magnitudes from the Paraficz et al. (2006) data to Tek2k was 16.29 mag; for the GLENDAMA data, it was 16.91 mag. Since the light curves from the literature used different calibration stars and all of the detectors have different quantum efficiency curves, we tested for photometric color terms, finding image A and B offsets of −0.013 and −0.002 mag for *OneChip*, −0.0104 and −0.0177 mag for GLENDAMA, and 0.0708 and 0.0127 mag for the Paraficz et al. (2006) data. We shifted the data points for image A (the less variable image) using a linear interpolation scheme to align with B, based on the measured time delay (16 days) from Paraficz et al. (2006), and then divided the two light curves to yield a time-delay-shifted "difference light curve," in which only variability extrinsic to the source (viz. microlensing) remains. The total combined light curves, displayed in Figure 3, comprise 186 epochs of data over a 16 yr monitoring period.

2.2. NIR

The *H*-band observations were taken with ASTROCAM (Fischer et al. 2003) on the 1.55 m reflector at NOFS. ASTROCAM employs an InSb detector spanning 1024 × 1024 pixels, with a $0\farcs366$ pixel scale. To mitigate sky saturation, $10''$ dithering between observations was applied. For each observing epoch, 108 such subexposures were taken, providing an effective exposure length of 400 s. Unusable images were identified by a poor PSF fit (reduced $\chi^2 > 1.5$), a seeing value $\geqslant 1\farcs3$, or by other complications in the data collection pipeline (bad rotations, doubled images, incomplete dithers, etc.); 41 exposures were found to be unsuitable for analysis. The cleaned *H*-band light curve consists of 27 epochs over 5 yr (2013–2018). The light curves for images A and B are shown in the top and bottom of Figure 3 respectively, and the observations are listed in Table 2.

We complete the NIR data reduction as in Cornachione et al. (2020a). To model the sky background, a twelfth-order Legendre polynomial with smooth variations was fit to pixel rows and columns to mask cosmic rays, defects in the detector, and stars, then subtracted from the image before flat-fielding. We fit each individual exposure for the fluxes in image A and image B, using the same reference stars as in the optical to find the PSF and flux normalizations, and we maintain a constant galaxy flux at each observing epoch. Again, the astrometry for the lens galaxy and quasar images was fixed to that from the HST *H*-band image. In the final light curves, the flux for every night is computed by a weighted average of the corresponding fluxes from that night's subexposures. Example images from our NIR reduction pipeline showing the original image, model, and residuals are shown in Figure 4. The flux error for each night is calculated from those of the corresponding

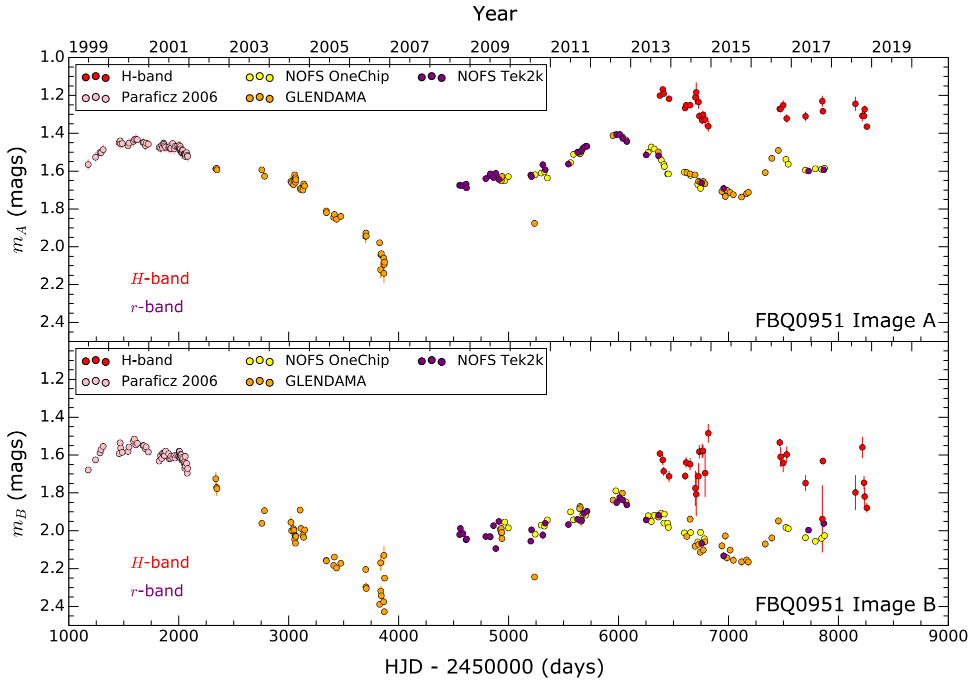

Figure 3. H-band (red) and r-band light curves for images A (top) and B (bottom) for FBQ0951. In the r-band light curve, the purple points represent NOFS Tek2k data, the yellow NOFS *OneChip* data, the orange GLENDAMA data, and the pink data are from Paraficz et al. (2006). The light curves are vertically offset for ease of comparison.

Table 2
H-Band Light Curves for FBQ J0951+2635 (NOFS)

HJD-2450000 (days)	Image A (mag)	Error A (mag)	Image B (mag)	Error B (mag)	Seeing (arcsec)
6376.649	4.052	0.006	4.973	0.015	0.834
6402.728	4.019	0.010	5.006	0.025	0.866
6410.710	4.042	0.009	5.066	0.022	0.936
6459.654	4.069	0.011	5.093	0.028	1.128
6605.947	4.118	0.008	5.091	0.019	0.798
6614.998	4.103	0.011	5.020	0.025	0.837
6651.031	4.103	0.013	5.029	0.030	0.935
6698.790	4.061	0.037	5.156	0.092	0.922
6706.831	4.035	0.052	5.188	0.116	0.844
6727.726	4.086	0.034	5.093	0.069	1.116
6734.722	4.160	0.017	4.963	0.035	1.249
6760.669	4.183	0.018	4.960	0.037	1.148
6767.719	4.154	0.021	4.958	0.030	0.787
6787.719	4.178	0.040	5.076	0.125	0.895
6816.683	4.214	0.027	4.866	0.049	1.248
7466.724	4.122	0.008	4.915	0.018	0.975
7473.794	4.122	0.017	4.990	0.052	0.901
7497.710	4.103	0.024	5.023	0.048	0.867
7529.696	4.173	0.020	4.978	0.041	1.046
7700.998	4.162	0.023	5.129	0.040	1.088
7853.818	4.082	0.028	5.318	0.177	1.302
7858.796	4.135	0.008	5.012	0.016	0.779
8201.739	4.172	0.015	5.019	0.032	0.826
8217.748	4.159	0.027	4.94	0.056	1.399
8232.766	4.160	0.014	5.127	0.035	0.837
8238.722	4.125	0.018	5.200	0.047	1.054
8258.720	4.216	0.009	5.260	0.023	1.022

(This table is available in machine-readable form.)

subexposures i by taking the weighted average following $\sigma = \sum_i \sqrt{1/\sigma_i^2}$. We tested our photometry for occurrences of flux from image A contaminating our measurement of the flux of image B. In these cases, we computed an additional systematic uncertainty term, whose magnitude was determined by the severity of the contamination. We added this additional uncertainty to the photometric errors in quadrature.

3. Modeling

3.1. Models for Strong Lensing

We used the GRAVLENS package (Keeton 2001) to model the mass profile of the lens galaxy. Since the lens galaxy in FBQ0951 is an edge-on spiral, we assembled a three-component model for the bulge, disk, and dark matter halo using a de Vaucouleurs profile, exponential disk, and Navarro, Frenk, and White (NFW; Navarro et al. 1997) dark matter profile, respectively. The parameters we use for the galaxy astrometry and profile fitting (determined by Lehár et al. 2000 using HST CASTLES imaging) are given in Table 3. In order to account for the unknown dark matter mass fraction, we created a sequence of 10 models, in which 0.1–1.0 of the macro model's mass is provided by the baryonic component, in steps of 0.1. These models permit us to examine a range of shear values and stellar to total convergence ratios (κ_*/κ), which are shown in Schechter & Wambsganss (2002) and Vernardos & Fluke (2014a), to strongly impact microlensing statistics. The mass fraction between the bulge and disk was held at a constant value of 0.3 (consistent with an Sa-/Sb-type galaxy; Graham & Worley 2008). Because the exponential disk is not a uniform mass to light ratio model, we define and use the fraction of baryonic to total surface mass density ($\Sigma_{\rm bary}/\Sigma_{\rm tot}$) at a specified image location, instead of the traditional value of $f_{M/L}$, to distinguish between our models and explore the fraction of baryonic matter within the galaxy. We forced all three

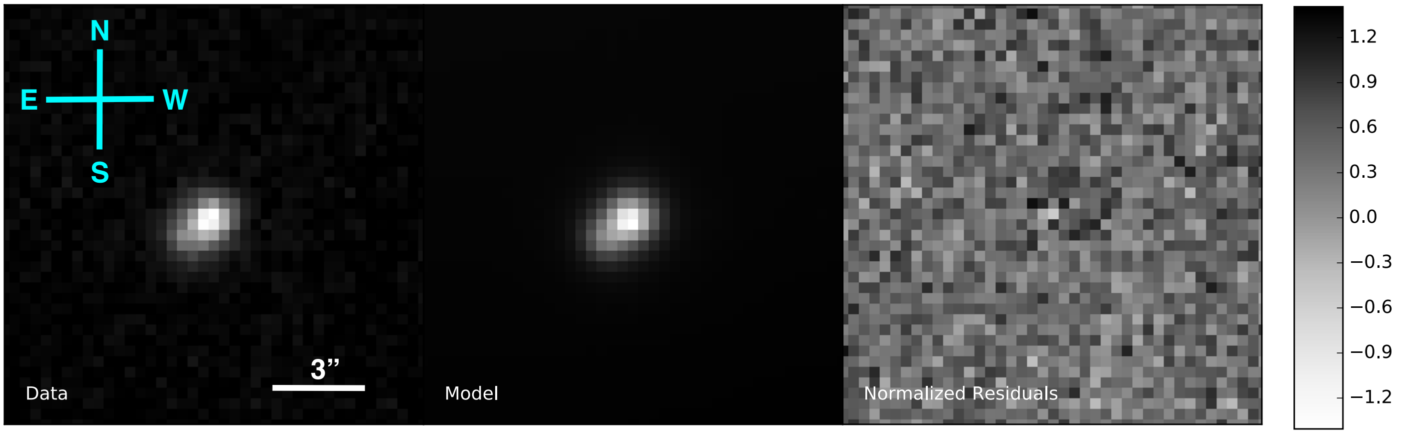

Figure 4. From left to right, the *H*-band background-subtracted data, model, and residuals for a fit to a subexposure of FBQ0951 taken on 2016 March 19.

components to be concentric, but we allowed the galaxy position, ellipticity, and position angle to float within the bounds of the observational uncertainties. The ellipticity is defined as $1 - \frac{b}{a}$ and the position angle is measured between the celestial meridian and the semimajor axis of the lens galaxy in degrees east of north. The free parameters of the model include the dark matter mass and the external shear. The values of the output shear (γ), convergence (κ), and stellar convergence fraction (κ_*/κ) for each of our 10 models are shown in Table 4.

The complexity of the three-component model led to some interesting trends in the sequence. Since most of the surface density in the location of image A is from the dark matter halo component, the convergence $\kappa = \Sigma/\Sigma_{\rm crit}$ decreases in a mostly monotonic manner as the total mass of the dark matter halo is reduced. The exception to this occurs in the “middle” of our model sequence, when all three components of the model begin to contribute significantly. In this portion of the model sequence, the χ^2 surface is relatively flat, leading to some degeneracy in the contributions of the model components.

The conditions in the vicinity of image B are more complex. In the low-κ^*/κ models, the cuspy NFW model is the dominant contributor to the convergence κ, and in the high-κ^*/κ case, the bulge and disk contribute very high surface densities to the convergence. The net effect is that the convergence is nearly equal in the “mostly dark matter” or “all stars” cases, but the degeneracy in the intermediate cases allows the model some freedom between the components, albeit over a reasonable range of parameter space.

3.2. Magnification Pattern

Magnification maps are created using the inverse ray-shooting technique of Wambsganss (1999). Every magnification pattern extends across a stellar mass range with a maximum to minimum ratio of 50 with $dN/dM \propto M^{-1.3}$, consistent with the Galactic initial mass function (IMF) of Gould (2000). The average microlens mass (the average mass of a star in the lens galaxy) $\langle M_*/M_\odot \rangle$ is left to be inferred during the Monte Carlo analysis phase. The magnification maps were 8192×8192 pixels, with a scale of $40 R_E$ ($2.71 \times 10^{18}\ \langle M_*/M_\odot \rangle^{1/2}$ cm) per side, where R_E is the Einstein Radius of a lens galaxy star with mean mass $\langle M_* \rangle$. For FBQ0951, R_E is $6.78 \times 10^{16}\ \langle M_*/M_\odot \rangle^{1/2}$ cm. The pixel scale ($3.31 \times 10^{14}\ \langle M_*/M_\odot \rangle^{1/2}$ cm) and the dimensions of the image were chosen to (1) permit resolution of the accretion disk at the small end of our range of trial source sizes and (2) allow ample room for constraining the large end of our trial source size distribution over the full duration of our (very long) light curves. Any plausible influences from systematics in the patterns were eliminated by the large number of realizations of the magnification patterns, with 40 per macro model for a total of 800 magnification patterns.

4. Microlensing

4.1. Optical Microlensing

We analyze the microlensing variability following the methods outlined in Kochanek (2004), in which Monte Carlo simulations are used to determine the set of physical parameters that were most likely to have produced the extrinsic variability in the observed light curves. To begin, we convolve a Gaussian kernel with the magnification patterns at a range of source sizes:

$$I(R) \propto \exp(-R^2/2r_s^2) \tag{1}$$

in the range $\log(\hat{r}_s/{\rm cm}) = [14.5, 18.5]\ \langle M_*/M_\odot \rangle^{1/2}$ cm, using 17 even intervals in logarithmic space, where r_s is the scale radius of the accretion disk at the rest-frame center of the monitoring band and $\hat{r}_s$ is the scale radius in Einstein units $\hat{r}_s = r_s \langle M_*/M_\odot \rangle^{-1/2}$. Then we test various trajectories across the convolved patterns in an attempt to recreate the observed light curves, since the magnification of the quasar’s continuum flux changes with the relative motion across the line of sight to the quasar. Mortonson et al. (2005) and Vernardos & Tsagkatakis (2019) found that the microlensing fluctuations are primarily dependent on the half-light radius $r_{1/2}$ and not on the specifics of the surface brightness profile, so we use a Gaussian profile for computational efficiency when performing those convolutions. For each trajectory, we randomly choose an effective velocity from a different initial position on the magnification map, under the assumption that these positions are uniformly distributed and independent. We use a log-uniform prior on $\hat{v}_e$, extending from $[10, 10^6]\ \langle M_*/M_\odot \rangle^{1/2}$ km s^{-1}. To minimize run time, we evaluate the reduced χ^2 (χ^2 per degree of freedom) during the simulations and abort any trial with a reduced $\chi^2 > 2.5$, since these trials will not contribute meaningful statistical weight to the Bayesian integrals. The

Table 3
Astrometry and Photometry for FBQ J0951+2635

Component	ΔR.A. (arcsec)	ΔDecl. (arcsec)	Scale Radius (arcsec)	Ellipticity $(1-\frac{b}{a})$	Position Angle (degrees)	F160W (mag)
Image A	0.000	0.000	...	...	...	15.62 ± 0.04
Image B	0.900 ± 0.003	−0.635 ± 0.003	...	...	...	16.99 ± 0.03
Galaxy Disk (Exponential Disk)	0.760 ± 0.003	−0.455 ± 0.003	0.37 ± 0.08	0.77 ± 0.07	13 ± 1	18.50 ± 0.30
Galaxy Bulge (de Vaucouleurs Profile)	0.760 ± 0.003	−0.455 ± 0.003	0.19 ± 0.06	0.2 ± 0.19	17 ± 25	17.86 ± 0.23

Note. Astrometry as reported by Lehár et al. (2000), using HST CASTLES imaging. Image A was used as the position reference.

Table 4
FBQ J0951+2635 Lens Galaxy Model Sequence

				Convergence			
$\Sigma_{\mathrm{bary}}/\Sigma_{\mathrm{tot}}$		κ_*/κ		κ		Shear γ	
A	B	A	B	A	B	A	B
0.02	0.24	2.85E-3	0.10	0.64	1.15	0.19	0.33
0.06	0.43	3.89E-3	0.20	0.56	1.13	0.23	0.50
0.10	0.59	7.37E-3	0.32	0.44	1.05	0.23	0.61
0.14	0.68	0.01	0.42	0.39	1.09	0.34	0.84
0.21	0.77	0.02	0.54	0.31	1.06	0.38	1.00
0.22	0.78	0.02	0.55	0.36	1.26	0.64	1.39
0.29	0.84	0.03	0.64	0.29	1.25	0.70	1.57
0.41	0.90	0.04	0.75	0.19	1.21	0.73	1.72
0.65	0.96	0.11	0.89	0.09	1.15	0.75	1.86
1.00	1.00	1.00	1.00	0.01	1.14	0.81	2.04

Monte Carlo code was run using The ARC[5] high-performance cluster at the United States Naval Academy; we attempted 100,000,000 trials per magnification pattern and 4.7×10^9 (5.88%) successfully met our reduced χ^2 cut.

Following this step, we utilize Bayesian statistics to examine the reduced χ^2 statistics of the fits to the observed light curves and determine likelihood functions for physical variables of interest, such as the system's transverse velocity and the source size of the quasar. Because this problem is characterized by multiple unknowns, we calculate the probability density for each variable of interest by marginalizing over the other variables in the model, utilizing priors covering the expected ranges for each parameter—for example, the probability density for the effective source velocity $\hat{v}_e$,

$$P(\hat{v}_e|D) \propto \int P(D|\hat{v}_e, \xi)\pi(\xi)\pi(\hat{v}_e)d\xi, \qquad (2)$$

with ξ representing all the other variables, including the fraction of baryonic to total matter surface mass density ($\Sigma_{\mathrm{bary}}/\Sigma_{\mathrm{tot}}$, where $\Sigma_{\mathrm{tot}} = \Sigma_{\mathrm{bary}} + \Sigma_{\mathrm{DM}}$) and the source radius $\hat{r}_s$. $\pi(\xi)$ represents the statistical priors we apply during the Bayesian integration.

4.2. NIR Microlensing

There are too few data points in the H-band light curve to permit a tight constraint on the size in this band if the light curve were analyzed on its own. This is because the fewer data points there are in the light curve, the larger the number of combinations of lensing parameters that are able to recreate the general trend of the light curve. Similar to the procedure used in Cornachione et al. (2020a), the H-band difference light curves are only fit to those r-band solutions that met the reduced χ^2 threshold. For these optical solutions, we repeat the procedure outlined in Section 4.1, to yield 1.5×10^5 (0.003%) successful joint fits to the r- and H-band light curves, restricted by a new reduced χ^2 limit of 3 on the NIR portion of the fits, since there were many fewer data points in the NIR light curve. In Figure 5, we display the best 10 simulated r-band (top) and H-band (bottom) difference light curves for FBQ0951.

5. Results

5.1. Microlensing Sizes, Mass, and Velocity

We follow the method of Kochanek (2004; specifically as implemented in Equation (5) of Mosquera & Kochanek 2011) to develop a model for the true effective transverse velocity between source, lens, and observer v_e, including the lens galaxy velocity dispersion σ_*, the bulk motion for the source and the lens $\sigma_{\mathrm{pec}(z_s)}$ and $\sigma_{\mathrm{pec}(z_l)}$, and the projection of the observer's velocity across the line of sight to the target v_{CMB}. We estimated σ_* using the mass from a Singular Isothermal Sphere model of the lens. We used the projection of the cosmic microwave background dipole along the line of sight to FBQ0951 to calculate the north and east components of the observer's velocity across the line of sight, finding 115 km s^{-1} and −204 km s^{-1}, respectively. We estimated the peculiar velocity of the quasar using the models of Tinker et al. (2012), finding $\sigma_{\mathrm{pec}}(z_s) = 112$ km s^{-1} and $\sigma_{\mathrm{pec}}(z_l) = 462$ km s^{-1}. We plot the probability density for this velocity model in Figure 6.

Convolving the source velocity probability density with our velocity model permits a calculation of the $\langle M_*/M_\odot\rangle$ distribution (shown in Figure 7),

$$P(\langle M_*/M_\odot\rangle|D) \propto \int P(\hat{v}_e|D)P(v_e)dv_e, \qquad (3)$$

since $\hat{v}_e = v_e\langle M_*/M_\odot\rangle^{-1/2}$. The 1σ interval for the mean microlensing mass is $0.072^{+0.37}_{-0.06}M_\odot$.

In Figure 8, we show the probability density for our primary result, the source size $\hat{r}_s = r_s\langle M_*/M_\odot\rangle^{-1/2}$ (given in Einstein units, scaled using a median stellar mass of $1M_\odot$ for the lens galaxy). To instead acquire the source radius in centimeters, one must convolve the $\hat{r}_s$ distribution with the probability density for $\langle M_*/M_\odot\rangle$. The resulting probability distributions (scaled to a half-light radius and corrected for an assumed 60° inclination angle $r_{s\ \mathrm{scaled}} = r_s\cos(i)^{-\frac{1}{2}}$) are shown in Figure 9 for the r and H bands. As a consistency check on the validity of our model for the transverse velocity v_e, we also calculated an estimate for the source size in physical units r_s, assuming a uniform prior on the average microlens mass $0.1 \leqslant \langle M_*/M_\odot\rangle \leqslant 1.0$. We also reran the simulations using GERLUMPH (Vernardos et al. 2014; Vernardos & Fluke 2014b) magnification maps, which have dimensions of

---

[5] https://www.usna.edu/ARCS/index.php

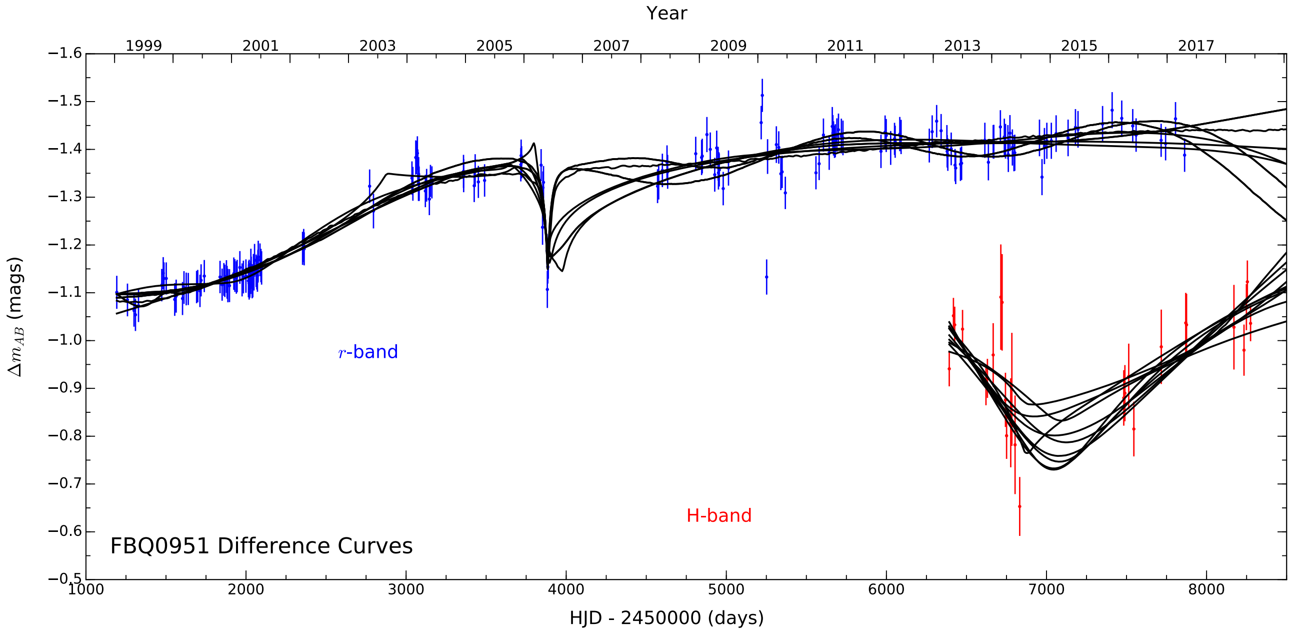

Figure 5. A representative sample of 10 simulated light curves (black) shown with the difference light curves in the *r* band (blue) and *H* band (red) for FBQ0951. Prior to creating the difference light curve, the image A light curve was shifted by the time delay. The two difference light curves are offset to allow for simultaneous viewing.

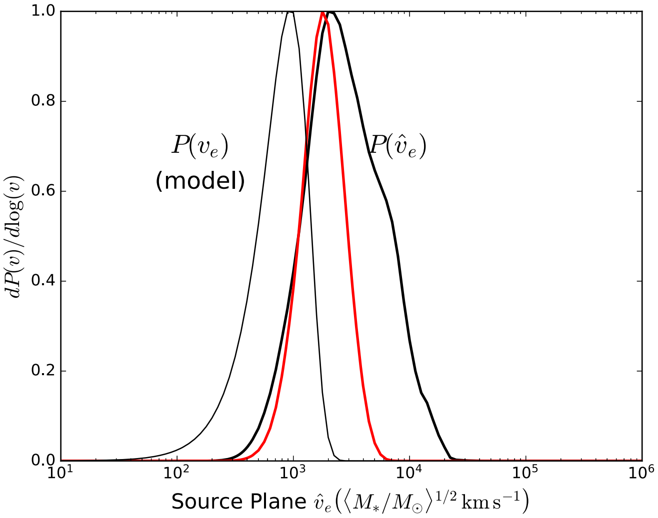

Figure 6. The probability density for effective velocity. The thicker curves in black and red, plotted in Einstein units in which $\hat{v}_e = v_e\langle M_*/M_\odot\rangle^{-1/2}$, show the probability density from the Monte Carlo simulations for the effective velocity in the optical and NIR, respectively. Our effective velocity model, which serves as the statistical prior on the effective velocity of the source, is plotted as a thin black curve in unscaled physical units (km s^{-1}). Note that analysis of the NIR curve disfavored some of the higher-velocity solutions derived from the optical, resulting in a narrower peak.

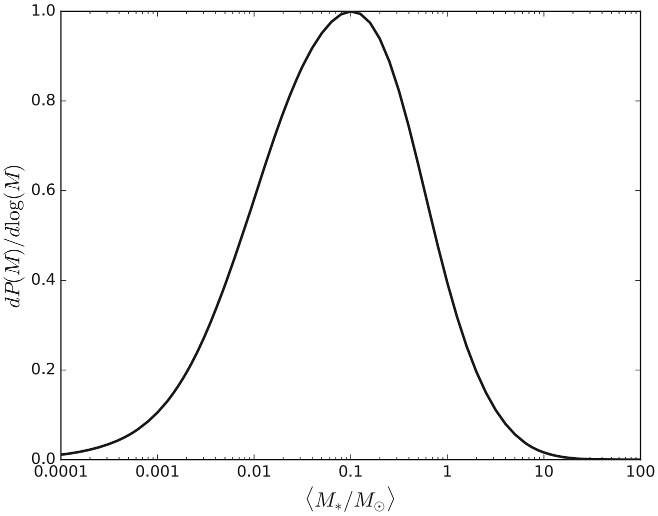

Figure 7. Mean microlens mass probability density found by convolving the $\hat{v}_e$ distribution with our model for the effective velocity of the source v_e.

25R$_\mathrm{E}$ by 25R$_\mathrm{E}$ and a single mean microlens mass. Both tests yielded consistent results, but it is notable to point out that the GERLUMPH magnification maps are constructed using a fixed microlens mass. The analysis of the light curves from this particular system therefore appears to be insensitive to the choice of IMF in the magnification patterns. The accretion disk sizes we measure are included in Table 5; for ease of comparison with other studies, we convert our values to a half-light radius and scale assuming a 60° inclination angle.

Our accretion disk size results are consistent in two separate and important ways. (1) As mentioned in the previous paragraph, the sizes we measure in both the *H* and *r* bands using our models for the transverse velocity v_e are fully consistent with those we found using a reasonable assumption for the mean mass of lens galaxy stars $0.1 \leqslant \langle M_*/M_\odot\rangle \leqslant 1.0$. (2) Furthermore, the *r*-band size we found using the joint *r*- and *H*-band analysis is consistent with, but considerably more precise than, the measurement yielded by the optical-only analysis. We promote the *r*-band measurement made using the joint light-curve analysis and the prior on the effective velocity v_e, $\log[r_{1/2}/\mathrm{cm}] = 16.24^{+0.33}_{-0.36}$ for the half-light radius of the accretion disk from the *r*-band emission at $\lambda_\mathrm{rest} = 2744$ Å, as our primary result, since it is more precise and because our velocity model has a much stronger physical basis than our simplistic prior on the microlens masses. Similarly, we choose the velocity-model-based *H*-band size measurement $17.04^{+0.26}_{-0.30}$

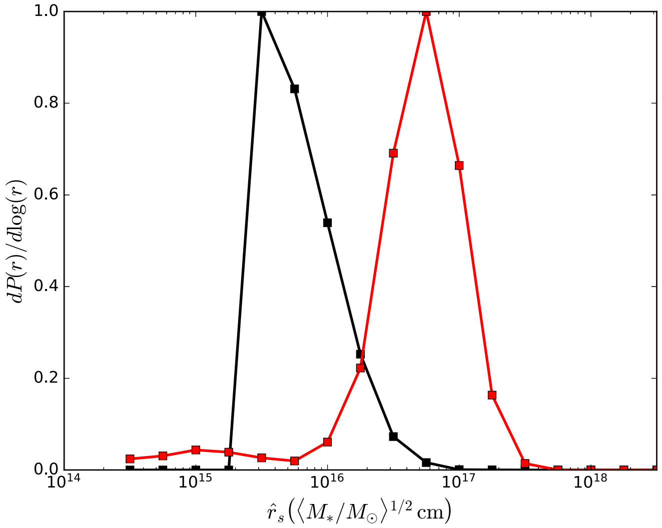

Figure 8. The scale radius probability density for the r band (black) and H band (red) given in Einstein units and scaled to a median microlensing mass of $1M_\odot$.

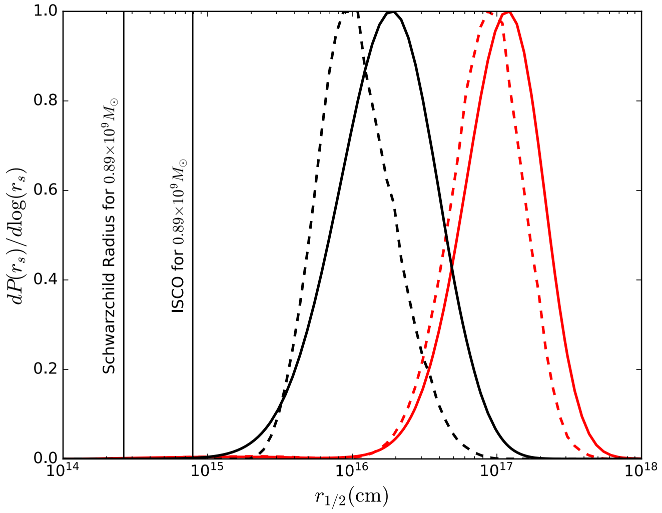

Figure 9. Probability density for the face-on half-light radius of the continuum source, assuming a 60° inclination angle $r_{1/2}$ (cm) in the r (black) and H (red) bands. The solid lines show the results without implementing a mass prior, while the dashed lines are the results when using a uniform mass prior from $[0.1,\ 1]M_\odot$. The vertical lines indicate the innermost stable circular orbit (ISCO) and Schwarzschild radius of the black hole (Peng et al. 2006).

Table 5
Microlensing Measurements of Accretion Disk Sizes

Filter	$\log[r_{1/2}/\mathrm{cm}]$	λ_{rest}	Single or Joint Fit
r	$16.58^{+0.38}_{-0.64}$	2744 Å	Single
r	$16.24^{+0.33}_{-0.36}$	2744 Å	Joint
H	$17.04^{+0.26}_{-0.30}$	7254 Å	Joint

Note. We report our accretion disk size measurements in half-light radii, assuming an inclination angle of 60°. Since our results are all self-consistent, we report our results without the mass prior applied. Joint fits were performed with both the H- and r-band data.

as our primary measurement of the size of this system's accretion disk at $\lambda_{\mathrm{rest}} = 7254$ Å.

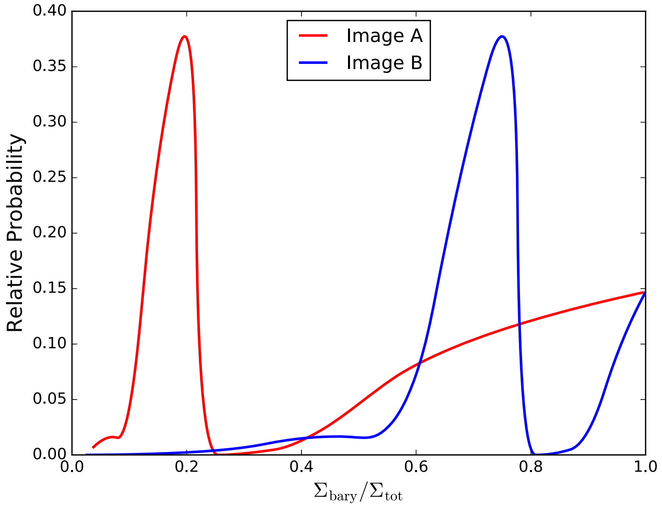

Figure 10. Relative probability of the baryonic surface density fraction $\Sigma_{\mathrm{bary}}/\Sigma_{\mathrm{tot}}$ at the positions of images A and B (in red and blue, respectively).

5.2. Surface Densities

We marginalized over the other variables of the simulation to yield a probability density for the lens galaxy macro model from our sequence, and we found a strong preference for models in the middle of our sequence, in which 40%–50% of the lens galaxy mass comes from the baryonic components. Given the complexity and underconstrained nature of the macro model, however, a plot showing the probability of the macro model as a function of the baryonic mass is difficult to interpret and not especially meaningful on its own. Since our three-component model is composed of smoothly distributed dark matter (the NFW component), a constant mass–light ratio bulge (the de Vaucouleurs component), and a disk of stars, gas, and dust (the exponential disk component), the surface density at the image locations is the extractable quantity with the most robust physical meaning, since microlensing statistics are strongly influenced by the ratio of the stellar to dark matter surface density at the image location (Schechter & Wambsganss 2002). In Figure 10, we display a plot showing the relative probability of the baryonic surface density fraction $\Sigma_{\mathrm{bary}}/\Sigma_{\mathrm{tot}}$, in which $\Sigma_{\mathrm{tot}} = \Sigma_{\mathrm{bary}} + \Sigma_{\mathrm{DM}}$, the sum of the surface density from the baryonic and dark matter components. Since image A is located outside the bulge and well away from the galactic plane, dark matter is the dominant surface density component in the preferred models of this region, $(\Sigma_{\mathrm{bary}}/\Sigma_{\mathrm{tot}})_A \approx 0.21$, but conditions are quite different at the location of image B in the disk, where the preferred model favors $(\Sigma_{\mathrm{bary}}/\Sigma_{\mathrm{tot}})_B \approx 0.77$. This is fully consistent with the findings of Schechter & Wambsganss (2002), in which the saddle point image (image B in the case of FBQ0951) is more likely to be significantly microlensed than the minimum image.

Compared to previous variability-based microlensing studies (with the possible exception of the study of PG 1115+080 by Morgan et al. 2008), this present investigation produced a more strongly defined preference for certain macro models. This is likely due to the unique geometry of the system: the lens galaxy is an edge-on spiral and the locations of the two quasar images in the disk (B) and halo (A) produce a large dynamic range in κ^*/κ. While this improved constraint was interesting, we were unfortunately unable to completely rule out solutions with unreasonably high baryonic mass fractions.

5.3. Accretion Disk Temperature Profile

Using the radii and rest wavelengths from Table 5, we measured the maximum likelihood fit in log-space to the function $\log(r_{1/2}) = (1/\beta)\log(\lambda) + C$ to find the slope β of the temperature profile $T(r) \propto r^{-\beta}$, yielding $\beta = 0.50^{+0.50}_{-0.18}$ for FBQ0951. Combining our present result with two other systems with microlensing variability-based measurements of the temperature profile (SBSJ0909+532 and QJ0957+561, from Cornachione et al. 2020a) yields a joint fit to the slope $\beta = 0.36^{+0.12}_{-0.07}$.

6. Discussion

Consistent with the findings of Cornachione & Morgan (2020), FBQ J0951+2635 is yet another system in which a microlensing variability study has yielded an accretion disk temperature profile that is shallower than that of standard thin-disk theory. As described in Section 1, single-epoch, chromatic microlensing studies have not converged on a consistent estimate for the temperature profile slope, so the empirical measurement of temperature profiles in additional systems remains a high priority.

In Section 1, we discuss the inconsistencies in accretion disk size measurements between multi-epoch microlensing measurements and the flux luminosity measurement when assuming a Shakura & Sunyaev (1973) thin-disk model (see also Cornachione & Morgan 2020 and the references therein), but Paic et al. (2022) have additionally pointed out that reverberation from the quasar's broad-line region (BLR) could be (falsely) interpreted as microlensing variability, potentially leading to biases in the variability-based size estimates as well. In this important work, Paic et al. (2022) found that continuum reverberation by the BLR resulted in high-frequency variations that carry information about the BLR size. They run comparisons between standard multi-epoch microlensing methods by comparing the power spectra of observed and simulated light curves in Fourier space. They find that confining their simulations to the low-frequency part of the power spectrum provided a radius estimate for QJ 0158-4325 that matches that of previous work (Morgan et al. 2012). Using all frequencies results in a smaller disk size, but the thin-disk model is only supported when they assume a very small microlens mass of $M = 0.01 M_{\odot}$. Paic et al. (2022) showed that in order to find a reasonable microlens mass with $M = 0.3 M_{\odot}$ for a thin-disk model, it is necessary to include BLR-induced continuum reverberation in their simulated light curves. However, they are not able to constrain the scale radius of the accretion disk with their model or make a measurement of the temperature slope of the disk, β, since their study was only performed in a single observing band. Nevertheless, the possibility of biases in our results from contaminating BLR flux is worth some consideration.

If it is true that incomplete modeling of BLR reverberation biases microlensing variability-based measurements toward larger sizes, is it possible that correction of this weakness could bring variability-based temperature profile estimates closer to the thin-disk model with $\beta = 0.75$? A bias that affected both the observed-frame optical and NIR size measurements equally would not change the temperature profile measurement at all, so a BLR reverberation bias would need to affect each size measurement differently in order to skew the slope measurement. It is plausible (and likely) that the amplitude of blended (big blue bump) BLR reverberation will be greater when caused by continuum flux at higher energies than at longer wavelengths, but this would bias the temperature profile constraint toward *steeper* slopes (larger β), since the rest-frame UV measurement would be biased more toward large sizes than would the rest-frame optical measurement. Therefore, it seems unlikely that our present, aggregate constraint on the temperature profile from QJ0957+561, SBSJ0909+523, and FBQ J0951+235, $\beta = 0.36^{+0.12}_{-0.07}$, has been biased toward shallower slopes (smaller β) by a failure to completely model the flux from the BLR. Nevertheless, for thoroughness, we also reran our full joint Monte Carlo simulation, simulating 30% contamination by flux from the larger, unmicrolensed BLR, but this did not cause any significant changes in our primary result. Our new measurement is consistent with, but more precise than, the measurement of Morgan et al. (2010), $\log(r_{1/2}/\mathrm{cm}) = 16.41^{+0.4}_{-0.4}$ (scaled here to a half-light radius at 2744 Å for a direct comparison with our results); the additional precision was made possible by the joint H- and r-band fit.

It is important to reiterate that our slope measurements are inconsistent with the simple thin-disk model, but many other accretion models produce shallower temperature profiles. Papadakis et al. (2022) are able to recreate the accretion disk sizes from gravitational lensing by modeling illumination of the accretion disk from the X-ray corona. Li et al. (2019) find that using a thin disk with a wind reconciles the disk size problem, as the wind would flatten the temperature profile. The expected β value from the slim-disk model of Abramowicz et al. (1988) is ∼0.5 for accretion rates $\geqslant 0.1$; this value of β is consistent with what has been found with multi-epoch microlensing studies. The interested reader should consult Cornachione & Morgan (2020) for a more in-depth discussion of the different physical models of the accretion disk that reproduce the observed temperature profiles determined from microlensing.

7. Summary and Conclusions

In this paper, we present multiple seasons of new r-band (10 seasons) and H-band monitoring data (five seasons) from NOFS of the gravitationally lensed quasar FBQ J0951+2635. We use these new data alongside observations from the literature to measure the size and temperature slope of the accretion disk, through microlensing simulations of these multi-epoch data. Our primary results are summarized below:

1. We find that the size of the accretion disk at an assumed inclination of 60° is $\log(r_{1/2}/\mathrm{cm}) = 16.24^{+0.33}_{-0.36}$ in the r band and $17.04^{+0.26}_{-0.30}$ in the H band, with the optical measurement being consistent with the value generated by Morgan et al. (2010).
2. We find that $\beta = 0.5^{+0.50}_{-0.18}$ for this system, which is nominally shallower, but still formally consistent with that expected from a Shakura & Sunyaev (1973) thin-disk model. However, a joint fit including the systems SBS0909 and Q0957 yields a value of $\beta = 0.36^{+0.12}_{-0.07}$, which is formally inconsistent with the Shakura & Sunyaev (1973) model.
3. Our analysis yields a more tightly constrained ratio of baryonic surface mass density to total surface mass density in the lens galaxy than previous studies.

Acknowledgments

We thank Bonnie Lucas and the USNA ARC team for their assistance in utilizing The ARC computing cluster for this work. This material is based upon work supported by the National Science Foundation under grant No. AST 2007680 to C.W.M.

ORCID iDs

Angelica B. Rivera https://orcid.org/0000-0001-8125-1669
Christopher W. Morgan https://orcid.org/0000-0003-2460-9999
Scott E. Dahm https://orcid.org/0000-0002-2968-2418
Matthew A. Cornachione https://orcid.org/0000-0003-1012-4771
Emilio E. Falco https://orcid.org/0000-0002-7061-6519

References

Abramowicz, M. A., Czerny, B., Lasota, J. P., & Szuszkiewicz, E. 1988, ApJ, 332, 646
Bate, N. F., Vernardos, G., O'Dowd, M. J., et al. 2018, MNRAS, 479, 4796
Blackburne, J. A., Pooley, D., Rappaport, S., & Schechter, P. L. 2011, ApJ, 729, 34
Cackett, E. M., Chiang, C.-Y., McHardy, I., et al. 2018, ApJ, 857, 53
Cornachione, M. A., & Morgan, C. W. 2020, ApJ, 895, 93
Cornachione, M. A., Morgan, C. W., Burger, H. R., et al. 2020a, ApJ, 905, 7
Cornachione, M. A., Morgan, C. W., Millon, M., et al. 2020b, ApJ, 895, 125
Dai, X., Kochanek, C. S., Chartas, G., et al. 2010, ApJ, 709, 278
Edelson, R., Gelbord, J., Cackett, E., et al. 2019, ApJ, 870, 123
Edelson, R., Gelbord, J. M., Horne, K., et al. 2015, ApJ, 806, 129
Eigenbrod, A., Courbin, F., & Meylan, G. 2007, A&A, 465, 51
Fischer, J., Vrba, F. J., Toomey, D. W., et al. 2003, Proc. SPIE, 4841, 564
Gil-Merino, R., Goicoechea, L. J., Shalyapin, V. N., & Oscoz, A. 2018, A&A, 616, A118
Goicoechea, L. J., Ullan, A., Ovaldsen, J. E., et al. 2006, arXiv:astro-ph/0609647
Gould, A. 2000, ApJ, 535, 928
Graham, A. W., & Worley, C. C. 2008, MNRAS, 388, 1708
Hainline, L. J., Morgan, C. W., Beach, J. N., et al. 2012, ApJ, 744, 104
Hainline, L. J., Morgan, C. W., MacLeod, C. L., et al. 2013, ApJ, 774, 69
Jiménez-Vicente, J., Mediavilla, E., Kochanek, C. S., et al. 2014, ApJ, 783, 47
Keeton, C. R. 2001, arXiv:astro-ph/0102340
Kochanek, C. S. 2004, ApJ, 605, 58
Kochanek, C. S., Morgan, N. D., Falco, E. E., et al. 2006, ApJ, 640, 47
Lehár, J., Falco, E. E., Kochanek, C. S., et al. 2000, ApJ, 536, 584
Li, Y.-P., Yuan, F., & Dai, X. 2019, MNRAS, 483, 2275
Morgan, C. W., Hainline, L. J., Chen, B., et al. 2012, ApJ, 756, 52
Morgan, C. W., Kochanek, C. S., Dai, X., Morgan, N. D., & Falco, E. E. 2008, ApJ, 689, 755
Morgan, C. W., Kochanek, C. S., Morgan, N. D., & Falco, E. E. 2010, ApJ, 712, 1129
Mortonson, M. J., Schechter, P. L., & Wambsganss, J. 2005, ApJ, 628, 594
Mosquera, A. M., & Kochanek, C. S. 2011, ApJ, 738, 96
Navarro, J. F., Frenk, C. S., & White, S. D. M. 1997, ApJ, 490, 493
Paic, E., Vernardos, G., Sluse, D., et al. 2022, A&A, 659, A21
Papadakis, I. E., Dovciak, M., & Kammoun, E. 2022, A&A, 666, A11
Paraficz, D., Hjorth, J., Burud, I., Jakobsson, P., & Elíasdóttir, Á. 2006, A&A, 455, L1
Peng, C. Y., Impey, C. D., Rix, H.-W., et al. 2006, ApJ, 649, 616
Peterson, B. M., Ferrarese, L., Gilbert, K. M., et al. 2004, ApJ, 613, 682
Poindexter, S., Morgan, N., & Kochanek, C. S. 2008, ApJ, 673, 34
Pooley, D., Blackburne, J. A., Rappaport, S., & Schechter, P. L. 2007, ApJ, 661, 19
Planck Collaboration, Aghanim, N., Akrami, Y., et al. 2020, A&A, 641, A6
Schechter, P. L., Gregg, M. D., Becker, R. H., Helfand, D. J., & White, R. L. 1998, AJ, 115, 1371
Schechter, P. L., & Wambsganss, J. 2002, ApJ, 580, 685
Shakura, N. I., & Sunyaev, R. A. 1973, A&A, 500, 33
Shalyapin, V. N., Goicoechea, L. J., Koptelova, E., et al. 2009, MNRAS, 397, 1982
Sluse, D., Hutsemékers, D., Courbin, F., Meylan, G., & Wambsganss, J. 2012, A&A, 544, A62
Tinker, J. L., Sheldon, E. S., Wechsler, R. H., et al. 2012, ApJ, 745, 16
Vernardos, G., & Fluke, C. J. 2014a, MNRAS, 445, 1223
Vernardos, G., & Fluke, C. J. 2014b, A&C, 6, 1
Vernardos, G., Fluke, C. J., Bate, N. F., & Croton, D. 2014, ApJS, 211, 16
Vernardos, G., & Tsagkatakis, G. 2019, MNRAS, 486, 1944
Wambsganss, J. 1999, JCoAM, 109, 353